Nano Research

ISSN 1998-0124 CN 11-5974/O4
https://doi.org/10.1007/s12274-020-3007-2

Research Article

Enhancement of oxygen reduction reaction activity by grain boundaries in platinum nanostructures

Enbo Zhu[1,2,§], Wang Xue[3,§], Shiyi Wang[4,§], Xucheng Yan[1], Jingxuan Zhou[1], Yang Liu[1], Jin Cai[1], Ershuai Liu[5], Qingying Jia[5], Xiangfeng Duan[3,6], Yujing Li[2], Hendrik Heinz[4] (✉), and Yu Huang[1,6] (✉)

[1] *Department of Materials Science and Engineering, University of California, Los Angeles, CA 90095, USA*
[2] *School of Materials Science and Engineering, Beijing Institute of Technology, Beijing 100081, China*
[3] *Department of Chemistry and Biochemistry, University of California, Los Angeles, CA 90095, USA*
[4] *Department of Chemical and Biological Engineering, University of Colorado Boulder, Boulder, CO 80309, USA*
[5] *Department of Chemistry and Chemical Biology, Northeastern University, Boston, MA 02115, USA*
[6] *California NanoSystems Institute, University of California, Los Angeles, CA 90095, USA*
[§] *Enbo Zhu, Wang Xue, and Shiyi Wang contributed equally to this work.*

Received: 11 July 2020 / **Revised:** 23 July 2020 / **Accepted:** 23 July 2020

ABSTRACT

Systematic control of grain boundary densities in various platinum (Pt) nanostructures was achieved by specific peptide-assisted assembly and coagulation of nanocrystals. A positive quadratic correlation was observed between the oxygen reduction reaction (ORR) specific activities of the Pt nanostructures and the grain boundary densities on their surfaces. Compared to commercial Pt/C, the grain-boundary-rich strain-free Pt ultrathin nanoplates demonstrated a 15.5 times higher specific activity and a 13.7 times higher mass activity. Simulation studies suggested that the specific activity of ORR was proportional to the resident number and the resident time of oxygen on the catalyst surface, both of which correlate positively with grain boundary density, leading to improved ORR activities.

KEYWORDS

oxygen reduction reaction, nanowire, peptide, grain boundaries

1 Introduction

Platinum (Pt)-based nanocatalysts have attracted intensive interest due to their promising applications in clean energy industries [1–7]. Particularly Pt-based nanomaterials have been considered as the most effective catalyst for oxygen reduction reaction (ORR) and are employed widely in proton exchange membrane fuel cell applications [8–13]. However, widespread commercial applications are constrained by the sluggish reduction kinetics of the cathodic ORR and the high cost of the Pt catalysts [14]. It has been demonstrated that the performance of catalysts strongly depends on the surface structures [15–20]. In particular, previous studies demonstrated that the catalytic structures rich in grain boundaries usually exhibit high catalytic activities, such as ORR, CO_2 reduction reaction (CO_2RR), and methanol oxidation reaction (MOR) [13, 21–24]. The grain boundaries can be developed inside polycrystalline crystals, but the density is usually scarce because of the consequent lattice distortion induced instability [25, 26]. On the other hand, abundant grain boundaries can be generated through the assembly of nanocrystals [27, 28]. To this end, biomimetic methods have been shown effective in guiding various assemblies taking examples from nature. With the help of biomolecules such as peptides, nanostructures rich in grain boundaries can be produced and regulated under rational design [27, 29–35].

Here we explored the assembly and coagulation of small Pt nanocrystals with the assistance of Pt-surface specific peptides to create grain-boundary-rich nanostructures. A positive quadratic correlation between the specific activity (SA) in ORR and the grain boundary density was observed among these Pt nanostructures. Impressively, the Pt ultrathin nanoplate exhibited much higher SA and mass activity (MA) in ORR compared to the commercial Pt/C and even some of the Pt alloys. Simulation studies indicated the superior ORR activities could be attributed to both the higher occurrence and the longer residence time of oxygen on the surface rich in gain boundaries.

2 Experimental

Pt nanoplates were synthesized under aqueous conditions and at room temperature in the presence of T7 peptide (Ac-TLTTLTN-$CONH_2$) [27, 32, 36]. In a typical synthesis, H_2PtCl_6, T7 peptide, $AlCl_3$, and H_2O were premixed in a reaction vial. The ascorbic acid solution was first introduced into the vial, followed by the injection of $NaBH_4$ solution. The final products were collected after 30 min. Please see the Electronic Supplementary Material (ESM) for experimental details.

Pt nanowires and Pt single-grain-boundary nanocrystals were synthesized under aqueous conditions and room temperature in the presence of BP7A peptide (Ac-TLHVSSY-$CONH_2$) [35–38]. H_2PtCl_6, K_2PtCl_4, BP7A peptide, and ascorbic acid were mixed with water. The mixed solution was stirred or vortexed,

Address correspondence to Yu Huang, yhuang@seas.ucla.edu; Hendrik Heinz, hendrik.heinz@colorado.edu

followed by the injection of $NaBH_4$ solution. The products were collected after 30 min of reaction. The Pt nanowires were obtained by 3,000 rpm vortex of the solution. The Pt single-grain-boundary nanocrystals were obtained with a reduced concentration of BP7A peptide. Please see the ESM for the experimental details.

3 Results and discussion

Pt ultrathin nanoplates, Pt nanowires, and Pt single-grain-boundary nanocrystals were synthesized with different densities of grain boundaries assisted by various specific peptides. The formation of Pt nanoplates and Pt nanowires was achieved through self-assembly of as-synthesized small Pt nanocrystals. Such assemblies generated abundant grain boundaries in the assembled structure with the thickness of the nanoplate/nanowire approaching the size of individual nanometer-sized grains (Figs. S1 and S2 in the ESM). Transmission electron microscopy (TEM) and high-resolution TEM (HRTEM) revealed that the Pt nanoplates exhibited 65 ± 9 nm edge lengths and 3.5 ± 0.1 nm plate thickness (Figs. 1(a) and 1(b)), while the Pt nanowires had an average diameter of 4.4 ± 0.3 nm (Figs. 1(c) and 1(d)). The Pt single-grain-boundary nanocrystals were 4.9 ± 0.9 nm in diameter with a grain boundary intersecting the nanocrystal (Fig. 1(e)). In comparison, the current state-of-the-art commercial Pt/C catalyst is 3.2 ± 0.8 nm in diameter and free of grain boundaries (Fig. 1(f)).

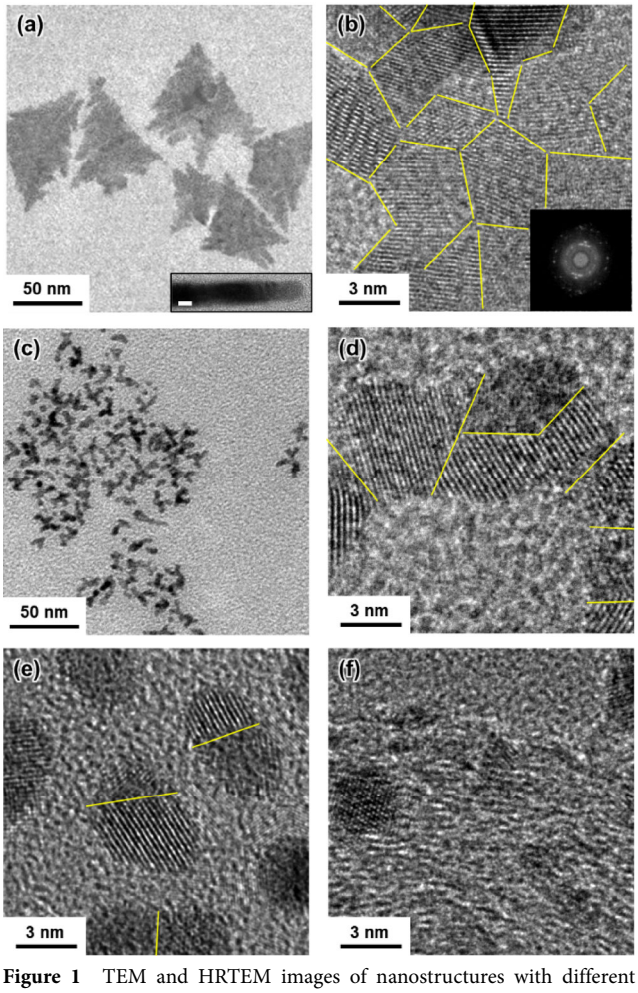

Figure 1 TEM and HRTEM images of nanostructures with different morphology and grain boundary densities. (a) TEM and (b) HRTEM of ultrathin Pt nanoplates. The inset of (a) is the side view of a nanoplate, and the scale bar is 2 nm. The inset of (b) is the FFT of (b), indicating the nanoplate is rich in grain boundaries. (c) TEM and (d) HRTEM of a Pt nanowire. (e) HRTEM of Pt single-grain-boundary nanocrystals. (f) HRTEM of commercial Pt/C. The grain boundaries in (b), (d), and (e) are marked with yellow lines for clarity.

To investigate the relationship between the ORR activities and the density of grain boundaries, the ORR performances of these Pt nanostructures were evaluated in comparison with the grain-boundary-free commercial Pt/C catalyst. As shown in the polarization curves (Fig. 2(b)), the onset potential of the Pt nanoplate was ~ 0.99 V (all potentials reported here were versus the reversible hydrogen electrode (RHE)). It was higher than the ~ 0.96 V onset potential of the rest (Fig. 2(b)), indicating a higher ORR activity of the nanoplate. The electrochemical surface areas (ECSAs) displayed in Fig. 2(c) were estimated by measuring the charge associated with under potential deposition of hydrogen (see ESM for calculation details) in the cyclic voltammograms (Fig. 2(a)). The nanoplates had ultrathin two-dimensional (2D) morphology with rough surfaces, showing an ECSA of 59.55 m^2/g_{Pt}. The Pt nanowire exhibited an ECSA of 42.56 m^2/g_{Pt}. The commercial Pt/C with a small size (3.2 ± 0.8 nm in diameter) exhibited an ECSA of 65.33 m^2/g_{Pt}, while the Pt single-grain-boundary nanocrystal with a larger size (5.2 ± 0.9 nm in diameter) exhibited an ECSA of 43.54 m^2/g_{Pt}. The SAs and the MAs of the Pt nanostructures at 0.9 V were compared (Figs. 2(d) and 2(e)). Pt nanoplates showed the highest SA of 5.76 mA/cm^2 and the highest MA of 3.43 $mA/\mu g_{Pt}$, among all the samples. In comparison, Pt nanowires showed a SA of 0.85 mA/cm^2 and a MA of 0.36 $mA/\mu g_{Pt}$; Pt single-grain-boundary nanocrystals showed a SA of 0.75 mA/cm^2

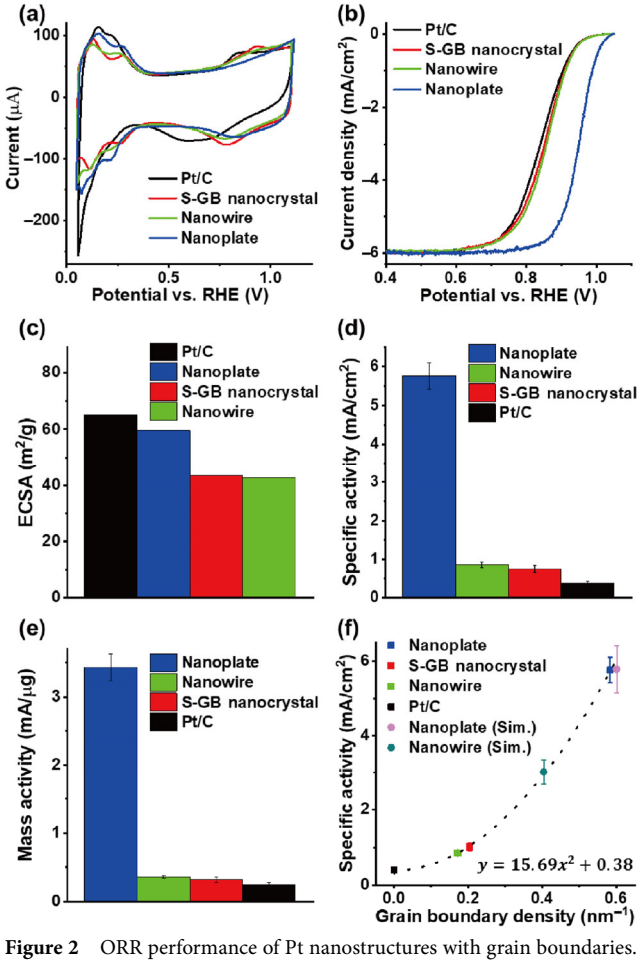

Figure 2 ORR performance of Pt nanostructures with grain boundaries. (a) The cyclic voltammograms and (b) ORR polarization curves. (c) ECSA of different nanostructures. (d) SAs and (e) MAs of different nanostructures. (f) The quadratic relationship between ORR SAs and the grain boundary densities. S-GB stood for single-grain-boundary. Samples with (Sim.) indicated those data were generated from the simulation.

and a MA of 0.32 mA/μg_{Pt}. Overall all of the synthesized Pt nanostructures showed higher ORR activities than those of the grain-boundary-free commercial Pt/C (SA: 0.38 mA/cm^2, MA: 0.25 mA/μg_{Pt}) (Table S1 in the ESM). Impressively, the ORR activity of Pt nanoplate was even better than some of the Pt-alloys (Table S2 in the ESM).

It was worth noting that no noticeable strain was observed in the grain-boundary rich Pt nanoplate when compared to bulk (extended X-ray absorption fine structure (EXAFS), Fig. S5 in the ESM). Hence the pronounced ORR activity is unlikely the result of strain effect as reported before [11].

As these assembled nanostructures were all made of Pt nanocrystals and there was no strain observed among the assembled nanostructures, we attribute the difference observed in ORR SAs to the varied grain boundary density expressed on the surface of these Pt nanostructures. Schematic models were established to estimate the grain boundary densities in different morphology of the nanostructures (Figs. S1–S3 in the ESM). The grain boundary densities of ultrathin Pt nanoplates (0.584 nm^{-1}), Pt nanowires (0.172 nm^{-1}), Pt single-grain-boundary nanocrystals (0.204 nm^{-1}) and commercial Pt/C (0 nm^{-1}) were obtained from the calculations of experimental data (see ESM for calculation details). The ORR SAs were then plotted versus the grain boundary densities. We note there the SA for single-grain-boundary nanocrystals was corrected to reflect grain boundary specific SA (see ESM for details). A positive quadratic correlation was observed and fitted as $y = 15.69\ x^2 + 0.38$, where y is the SA in mA/cm^2 and x is the grain boundary density in nm^{-1} (Fig. 2(f)). The result clearly indicated that the structures with more grain boundaries exhibited higher activities towards ORR.

To understand the role grain boundaries played in enhancing ORR activities, molecular dynamics simulations were performed to analyze the oxygen residence on the surfaces on the molecular scale. We employed large-scale atomic/molecular massively parallel simulator (LAMMPS) [39] and the INTERFACE force field (IFF) that cover parameters for inorganic and organic compounds, based on a classical Hamiltonian and thermodynamically consistent Lennard-Jones (LJ) parameters for face-centered cubic (FCC) metals [40, 41] and gas molecules (see ESM for computational details). Slab models were built to represent Pt {111} single nanocrystal surfaces (Fig. 3(a)), and Pt nanocrystal surfaces with grain boundaries including one-dimensional (1D) Pt nanowires (Fig. 3(c)) and two-dimensional (2D) Pt nanoplates (Fig. 3(e)), and then the models were relaxed to reach a stable state. 88 oxygen molecules were then placed into each lattice of the model to examine their residence. Oxygen molecules with neighboring platinum atom within 3.5 Å distance were regarded as a resident molecule (see ESM for analysis details). The simulation time was 55 ns, and the spatial distribution of oxygen molecules reached stable equilibrium for all three Pt structures in less than 10 ns (Fig. S6(a) in the ESM).

After the oxygen molecules reached a stable residence equilibrium (10 to 55 ns), the average number of oxygen molecules resident on the surface of grain-boundary-rich nanowires and nanoplates was (0.154 ± 0.039)/nm^2 and (0.147 ± 0.032)/nm^2 respectively, which was 2.24 and 2.14 times higher than the average number of (0.069 ± 0.017)/nm^2 oxygen molecules resident on the single-crystal surface (Fig. 3(b)). The resident time of the oxygen on the surface for each oxygen molecule was given in Fig. S6(b) in the ESM. On average, the resident time for oxygen on the surface of grain-boundary-rich nanowires and nanoplates was 4.37 and 8.77 ns respectively, which was 3.50 and 7.02 times of the 1.25 ns for an oxygen resident on the single-crystal surface (Fig. 3(d)). The results indicated that

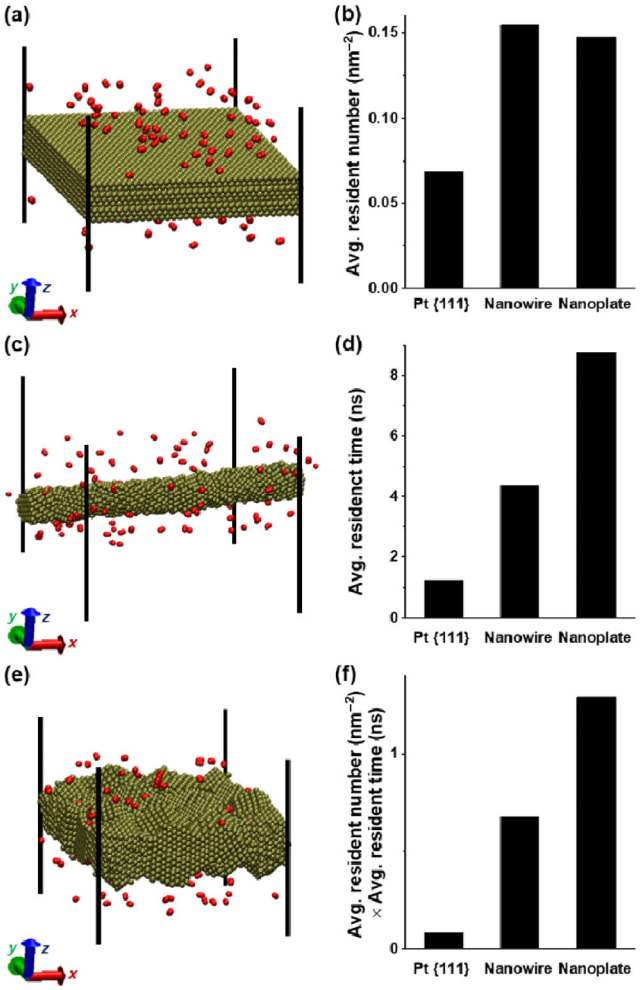

Figure 3 Oxygen residence on different Pt surfaces with and without grain boundaries from the simulation. Slab lattices were built for Pt {111} surface free of grain boundary (a), Pt nanowire rich in grain boundaries (c), and Pt nanoplate rich in grain boundaries (e). The representative snapshots were in VDW representation with the periodic boxes indicated. Water molecules are hidden for visual clarity. (b) The average number of oxygen molecules resident on Pt surfaces in different structures. (d) The average residence time of oxygen molecules on Pt surfaces in different structures. (f) The product of the average oxygen resident number and the average oxygen resident time in different structures.

the grain boundary could dramatically enhance the chance and the lifetime of the oxygen residence, thereby improving the ORR activity. The coordination number of the atoms at the grain boundaries was relatively low and the atom arrangement was highly disturbed due to the disruption of the periodicity. As a result, compared to a perfect single crystal surface, the residence of oxygen molecules was more accessible, and the residence time was longer at these grain boundary sites.

To further understand the roles of the oxygen residence on ORR SA, we examined the ORR SA that is expressed in the Arrhenius equation as

$$SA = Ae^{\frac{-E_a}{RT}}$$

Where R was the gas constant, T was the temperature, E_a was the activation energy and A was the preexponential factor. E_a was suggested to vary little in the ORR on different Pt surfaces [42, 43]. If this is also the case here, then the preexponential factor A should determine the SA. As A is generally thought to relate to the local concentrations of reactants [42], we suggest herein that A will be proportional to both the resident number and the resident time of oxygen on the Pt surface. Indeed, the

multiplication of the average resident number and the average resident time of oxygen on the surfaces of different structures resulted in 7.86 and 15.02 times enhancement of oxygen residence on grain-boundary-rich nanowires and nanoplates, respectively, compared to that of the single-crystal surface (Fig. 3(f)). Taken that the SA of single-crystal Pt/C is 0.38 mA/cm^2, and therefore we estimate the theoretical SAs for simulated nanoplates and nanowires to be 5.78 and 3.02 mA/cm^2, respectively. The estimated theoretical SAs and the simulated grain boundary densities (nanoplate: 0.601 nm^{-1} and nanowire: 0.404 nm^{-1}) (Fig. S4, see ESM for calculation details) fitted nicely with the experimental plot we achieved (Fig. 2(f)). This suggested that the ORR SA on the strain-free grain-boundary-rich surface was proportionally enhanced by higher oxygen resident number and longer oxygen resident time, which likely correlates to higher oxygen concentration around the grain boundaries.

On the other hand, grain boundaries may favor the oxidation of Pt and negatively impact the durability of the catalysts [44]. Indeed, a strong oxidation peak was observed in the EXASF for Pt nanoplates (Fig. S5 in the ESM). And after the 30 K durability test, Pt nanoplates showed a larger percentage drop in MA than that of the commercial Pt/C (Figs. S5(a) and S7 in the ESM). This issue can be however circumvented by lining the grain boundaries with Pd (Fig. S8 in the ESM), where the Pt oxidation peak was found greatly suppressed in Pd-doped Pt nanoplates (Fig. S5(b) in the ESM), leading to much better durability [27].

4 Conclusions

In summary, we synthesized different Pt nanostructures with different densities of grain boundaries with the assistance of specific peptides. The ORR SAs of these structures demonstrated a positive quadratic correlation with the exhibited grain boundary densities. With abundant grain boundaries, Pt ultrathin nanoplates exhibited greatly improved ORR SAs compared to commercial Pt/C. Pt nanoplates demonstrated a 15.5 times higher SA and a 13.7 times higher MA in ORR compared to Pt/C. It represented the highest activity enhancement of Pt-only catalysts over commercial Pt/C to date, without the use of lattice strain. Molecular dynamics simulation indicated the ORR SA was proportional to the oxygen resident number and the oxygen resident time on the catalyst surface, and both of them were greatly enhanced by the grain boundaries, leading to higher ORR activities.

Coupled with EXASF studies, we also showed that although grain boundaries led to oxidation of Pt and hence inferior stability, this problem can be addressed by suppressing Pt oxidation through depositing Pd along grain boundaries, leading to much-improved catalysts stability.

Collectively, this work demonstrated a systematic and rational control over the grain boundaries by biomimetic methods and quantified the impact of the grain boundaries on the ORR activity on Pt surfaces, which provided a feasible and new route to improve ORR activities via structural design without inducing strain.

Acknowledgements

E. Z. and Y. H. acknowledge the Electron Imaging Center of Nanomachines at University of California, Los Angeles for TEM support. Y. H. acknowledges support from the Office of Naval Research under grant number N000141812491 and National Science Foundation DMREF 1437263. S. W. and H. H. acknowledge support by the National Science Foundation (DMREF 1623947, CBET 1530790, OAC 1931587, and CMMI 1940335). The allocation of computational resources is acknowledged at the Argonne Leadership Computing Facility, which is a DOE Office of Science User Facility supported under contract DE-AC02-06CH11357, and at the Summit supercomputer supported by the National Science Foundation (ACI-1532235 and ACI-1532236). The authors declare no competing financial interests. Use of beamline ISS 8-ID of the National Synchrotron Light Source (NSLS) II was supported by the NSLS-II, Brookhaven National Laboratory, under U.S. DOE Contract No. DE-SC0012704.

Electronic Supplementary Material: Supplementary material (further details of the experiments, simulations, grain boundary analysis, TEM measurements, electrochemical measurements, etc.) is available in the online version of this article at https://doi.org/10.1007/s12274-020-3007-2.

References

[1] Strasser, P. Catalysts by Platonic design. *Science* **2015**, *349*, 379–380.

[2] Li, M. F.; Duanmu, K. N.; Wan, C. Z.; Cheng, T.; Zhang, L.; Dai, S.; Chen, W. X.; Zhao, Z. P.; Li, P.; Fei, H. L. et al. Single-atom tailoring of platinum nanocatalysts for high-performance multifunctional electrocatalysis. *Nat. Catal.* **2019**, *2*, 495–503.

[3] Wilson, N. M.; Pan, Y. T.; Shao, Y. T.; Zuo, J. M.; Yang, H.; Flaherty, D. W. Direct synthesis of H_2O_2 on AgPt octahedra: The importance of Ag-Pt coordination for high H_2O_2 selectivity. *ACS Catal.* **2018**, *8*, 2880–2889.

[4] Li, C. Z.; Liu, T. Y.; He, T.; Ni, B.; Yuan, Q.; Wang, X. Composition-driven shape evolution to Cu-rich PtCu octahedral alloy nanocrystals as superior bifunctional catalysts for methanol oxidation and oxygen reduction reaction. *Nanoscale* **2018**, *10*, 4670–4674.

[5] Liu, H. P.; Zhong, P.; Liu, K.; Han, L.; Zheng, H. Q.; Yin, Y. D.; Gao, C. B. Synthesis of ultrathin platinum nanoplates for enhanced oxygen reduction activity. *Chem. Sci.* **2018**, *9*, 398–404

[6] Lei, W. J.; Li, M. G.; He, L.; Meng, X.; Mu, Z. J.; Yu, Y. S.; Ross, F. M.; Yang, W. W. A general strategy for bimetallic Pt-based Nano-branched structures as highly active and stable oxygen reduction and methanol oxidation bifunctional catalysts. *Nano Res.* **2020**, *13*, 638–645.

[7] Huang, L. P.; Zhang, W.; Li, P.; Song, Y. B.; Sheng, H. T.; Du, Y. X.; Wang, Y. G.; Wu, Y. E.; Hong, X.; Ding Y. H. et al. Exposing Cu-rich {110} active facets in PtCu nanostars for boosting electrochemical performance toward multiple liquid fuels electrooxidation. *Nano Res.* **2019**, *12*, 1147–1153.

[8] Stephens, I. E. L.; Bondarenko, A. S.; Grønbjerg, U.; Rossmeisl, J.; Chorkendorff, I. Understanding the electrocatalysis of oxygen reduction on platinum and its alloys. *Energy Environ. Sci.* **2012**, *5*, 6744–6762.

[9] Wang, L.; Holewinski, A.; Wang, C. Prospects of platinum-based nanostructures for the electrocatalytic reduction of oxygen. *ACS Catal.* **2018**, *8*, 9388–9398.

[10] Stamenkovic, V. R.; Fowler, B.; Mun, B. S.; Wang, G. F.; Ross, P. N.; Lucas, C. A.; Marković, N. M. Improved oxygen reduction activity on $Pt_3Ni(111)$ via increased surface site availability. *Science* **2007**, *315*, 493–497.

[11] Li, M. F.; Zhao, Z. P.; Cheng, T.; Fortunelli, A.; Chen, C. Y.; Yu, R.; Zhang, Q. H.; Gu, L.; Merinov, B. V.; Lin, Z. Y. et al. Ultrafine jagged platinum nanowires enable ultrahigh mass activity for the oxygen reduction reaction. *Science* **2016**, *354*, 1414–1419.

[12] Huang, X. Q.; Zhao, Z. P.; Cao, L.; Chen, Y.; Zhu, E. B.; Lin, Z. Y.; Li, M. F.; Yan, A. M.; Zettl, A.; Wang, Y. M. et al. High-performance transition metal-doped Pt_3Ni octahedra for oxygen reduction reaction. *Science* **2015**, *348*, 1230–1234.

[13] Zhang, Z. C.; Luo, Z. M.; Chen, B.; Wei, C.; Zhao, J.; Chen, J. Z.; Zhang, X.; Lai, Z. C.; Fan, Z. X.; Tan, C. L. et al. One-pot synthesis of highly anisotropic five-fold-twinned PtCu nanoframes used as a bifunctional electrocatalyst for oxygen reduction and methanol oxidation. *Adv. Mater.* **2016**, *28*, 8712–8717.

[14] Nørskov, J. K.; Rossmeisl, J.; Logadottir, A.; Lindqvist, L.; Kitchin, J. R.; Bligaard, T.; Jónsson, H. Origin of the overpotential for oxygen reduction at a fuel-cell cathode. *J. Phys. Chem. B* **2004**, *108*, 17886–17892.

[15] Luo, M. C.; Zhao, Z. L.; Zhang, Y. L.; Sun, Y. J.; Xing, Y.; Lv, F.; Yang, Y.; Zhang, X.; Hwang, S.; Qin, Y. N. et al. PdMo bimetallene for oxygen reduction catalysis. *Nature* **2019**, *574*, 81–85.

[16] Tian, N.; Zhou, Z. Y.; Sun, S. G.; Ding, Y.; Wang, Z. L. Synthesis of tetrahexahedral platinum nanocrystals with high-index facets and high electro-oxidation activity. *Science* **2007**, *316*, 732–735.

[17] He, D. S.; He, D. P.; Wang, J.; Lin, Y.; Yin, P. Q.; Hong, X.; Wu, Y. E.; Li, Y. D. Ultrathin icosahedral Pt-enriched nanocage with excellent oxygen reduction reaction activity. *J. Am. Chem. Soc.* **2016**, *138*, 1494–1497.

[18] Ma, L.; Wang, C. M.; Gong, M.; Liao, L. W.; Long, R.; Wang, J. G.; Wu, D.; Zhong, W.; Kim, M. J.; Chen, Y. X. et al. Control over the branched structures of platinum nanocrystals for electrocatalytic applications. *ACS Nano* **2012**, *6*, 9797–9806.

[19] Liang, H. W.; Cao, X.; Zhou, F.; Cui, C. H.; Zhang, W. J.; Yu, S. H. A Free-standing Pt-nanowire membrane as a highly stable electrocatalyst for the oxygen reduction reaction. *Adv. Mater.* **2011**, *23*, 1467–1471.

[20] Zhou, S.; Zhao, M.; Yang, T. H.; Xia, Y. N. Decahedral nanocrystals of noble metals: Synthesis, characterization, and applications. *Materialstoday* **2019**, *22*, 108–131.

[21] Cheng, H.; Liu, S.; Hao, Z. K.; Wang, J. Y.; Liu, B. J.; Liu, G. Y.; Wu, X. J.; Chu, W. S.; Wu, C. Z.; Xie, Y. Optimal coordination-site exposure engineering in porous platinum for outstanding oxygen reduction performance. *Chem. Sci.* **2019**, *10*, 5589–5595.

[22] Zhang, T.; Bai, Y.; Sun, Y. Q.; Hang, L. F.; Li, X. Y.; Liu, D. L.; Lyu, X.; Li, C. C.; Cai, W. P.; Li, Y. Laser-irradiation induced synthesis of spongy AuAgPt alloy nanospheres with high-index facets, rich grain boundaries and subtle lattice distortion for enhanced electrocatalytic activity. *J. Mater. Chem. A* **2018**, *6*, 13735–13742.

[23] Gao, D. W.; Li, S.; Lv, Y. P.; Zhuo, H. Y.; Zhao, S.; Song, L. H.; Yang, S. H.; Qin, Y. C.; Li, C. C.; Wei, Q. et al. PtNi colloidal nanoparticle clusters: Tuning electronic structure and boundary density of nanocrystal subunits for enhanced electrocatalytic properties. *J. Catal.* **2019**, *376*, 87–100.

[24] Huang, H. W.; Ruditskiy, A.; Choi, S. I.; Zhang, L.; Liu, J. Y.; Ye, Z.; Xia, Y. N. One-pot synthesis of penta-twinned palladium nanowires and their enhanced electrocatalytic properties. *ACS Appl. Mater. Interfaces* **2017**, *9*, 31203–31212.

[25] Wu, J. B.; Qi, L.; You, H. J.; Gross, A.; Li, J.; Yang, H. Icosahedral platinum alloy nanocrystals with enhanced electrocatalytic activities. *J. Am. Chem. Soc.* **2012**, *134*, 11880–11883.

[26] Olmsted, D. L.; Foiles, S. M.; Holm, E. A. Survey of computed grain boundary properties in face-centered cubic metals: I. Grain boundary energy. *Acta Mater.* **2009**, *57*, 3694–3703.

[27] Zhu, E. B.; Yan, X. C.; Wang, S. Y.; Xu, M. J.; Wang, C.; Liu, H. T.; Huang, J.; Xue, W.; Cai, J.; Heinz, H. et al. Peptide-assisted 2-D assembly toward free-floating ultrathin platinum nanoplates as effective electrocatalysts. *Nano Lett.* **2019**, *19*, 3730–3736.

[28] Li, D. S.; Nielsen, M. H.; Lee, J. R. I.; Frandsen, C.; Banfield, J. F.; De Yoreo, J. J. Direction-specific interactions control crystal growth by oriented attachment. *Science* **2012**, *336*, 1014–1018.

[29] Chen, J. J.; Zhu, E. B.; Liu, J.; Zhang, S.; Lin, Z. Y.; Duan, X. F.; Heinz, H.; Huang, Y.; De Yoreo, J. J. Building two-dimensional materials one row at a time: Avoiding the nucleation barrier. *Science* **2018**, *362*, 1135–1139.

[30] Heo, K.; Jin, H. E.; Kim, H.; Lee, J. H.; Wang, E.; Lee, S. W. Transient self-templating assembly of M13 bacteriophage for enhanced biopiezoelectric devices. *Nano Energy* **2019**, *56*, 716–723.

[31] Chen, P. Y.; Hyder, M. N.; Mackanic, D.; Courchesne, N. M. D.; Qi, J. F.; Klug, M. T.; Belcher, A. M.; Hammond, P. T. Assembly of viral hydrogels for three-dimensional conducting nanocomposites. *Adv. Mater.* **2014**, *26*, 5101–5107.

[32] Zhu, E. B.; Wang, S. Y.; Yan, X. C.; Sobani, M.; Ruan, L. Y.; Wang, C.; Liu, Y.; Duan, X. F.; Heinz, H.; Huang, Y. Long-range hierarchical nanocrystal assembly driven by molecular structural transformation. *J. Am. Chem. Soc.* **2019**, *141*, 1498–1505.

[33] Lee, J.; Ju, M. S.; Cho, O. H.; Kim, Y.; Nam, K. T. Tyrosine-rich peptides as a platform for assembly and material synthesis. *Adv. Sci.* **2019**, *6*, 1801255.

[34] Chang, J. Y.; Wu, H. M.; Chen, H.; Ling, Y. C.; Tan, W. H. Oriented assembly of Au nanorods using biorecognition system. *Chem. Commun.* **2005**, 1092–1094.

[35] Ruan, L. Y.; Zhu, E. B.; Chen, Y.; Lin, Z. Y.; Huang, X. Q.; Duan, X. F.; Huang, Y. Biomimetic synthesis of an ultrathin platinum nanowire network with a high twin density for enhanced electrocatalytic activity and durability. *Angew. Chem., Int. Ed.* **2013**, *52*, 12577–12581.

[36] Chiu, C. Y.; Li, Y. J.; Ruan, L. Y.; Ye, X. C.; Murray, C. B.; Huang, Y. Platinum nanocrystals selectively shaped using facet-specific peptide sequences. *Nat. Chem.* **2011**, *3*, 393–399.

[37] Li, Y. J.; Huang, Y. Morphology-controlled synthesis of platinum nanocrystals with specific peptides. *Adv. Mater.* **2010**, *22*, 1921–1925.

[38] Ruan, L. Y.; Ramezani-Dakhel, H.; Lee, C.; Li, Y. J.; Duan, X. F.; Heinz, H.; Huang, Y. A rational biomimetic approach to structure defect generation in colloidal nanocrystals. *ACS Nano* **2014**, *8*, 6934–6944.

[39] Plimpton, S. Fast parallel algorithms for short-range molecular dynamics. *J. Comput. Phys.* **1995**, *117*, 1–19.

[40] Heinz, H.; Lin, T. J.; Kishore Mishra, R.; Emami, F. S. Thermodynamically consistent force fields for the assembly of inorganic, organic, and biological nanostructures: The interface force field. *Langmuir* **2013**, *29*, 1754–1765.

[41] Heinz, H.; Vaia, R. A.; Farmer, B. L.; Naik, R. R. Accurate simulation of surfaces and interfaces of face-centered cubic metals using 12–6 and 9–6 Lennard-Jones potentials. *J. Phys. Chem. C* **2008**, *112*, 17281–17290.

[42] Stamenković, V.; Schmidt, T. J.; Ross, P. N.; Marković, N. M. Surface composition effects in electrocatalysis: Kinetics of oxygen reduction on well-defined Pt_3Ni and Pt_3Co alloy surfaces. *J. Phys. Chem. B* **2002**, *106*, 11970–11979.

[43] Paulus, U. A.; Schmidt, T. J.; Gasteiger, H. A.; Behm, R. J. Oxygen reduction on a high-surface area Pt/Vulcan carbon catalyst: A thin-film rotating ring-disk electrode study. *J. Electroanal. Chem.* **2001**, *495*, 134–145.

[44] Lopes, P. P.; Tripkovic, D.; Martins, P. F. B. D.; Strmcnik, D.; Ticianelli, E. A.; Stamenkovic, V. R.; Markovic, N. M. Dynamics of electrochemical Pt dissolution at atomic and molecular levels. *J. Electroanal. Chem.* **2018**, *819*, 123–129.